Rapid Interactive Design–to–Performance of Mixed–Flow Space Inducers

Luca d'Agostino

（ *Civil and Industrial Engineering Department, University of Pisa, Pisa, Italy, luca.d'Agostino@ing.unipi.it* ）

Abstract： In this paper,the development and experimental validation of a reduced order model for preliminary design and noncavitating performance prediction of mixed- flow tapered- hub inducers for space propulsion applications is given. The model expresses the 3D incompressible, inviscid, irrotational flow in the blade channels by superposing a 2D axial vorticity correction to a fully- guided axisymmetric flow with radially uniform axial velocity. Suitable redefinition of the diffusion factor for bladings with non-negligible radial flow simultaneously allows for the control of the blade loading and the estimate of the boundary layer blockage and viscous blade losses at the specified design flow coefficient, providing a simple criterion for matching the hub profile to the axial variation of the blade pitch angle. Carter's rule is employed to account for flow deviation at the inducer trailing edge. Mass continuity, angular momentum conservation and the Euler equation are used to derive a simple 2nd order boundary value problem whose numerical solution defines the far- field axisymmetric flow velocity at the inducer discharge. The noncavitating pumping characteristic is then obtained using suitably adapted semi-empirical corrections for incidence, casing and tip clearance losses. The model has been verified to closely approximate the geometry and noncavitating head characteristics of two space inducers tested in the Cavitating Pump Rotordynamic Test Facility, as well as those of a number of tapered-hub inducers documented in the literature.

Keywords： Turbomachines, Turbopumps, Inducers, Aerospace Propulsion, Rocket Propulsion, Liquid Propellant Rocket Engines, Liquid Propellant Feed Turbopumps, Turbopump Inducer Hydrodynamics, Turbopump Inducer Geometry, Inducer Design and Performance Tool

Nomenclature

Latin Symbols

a distance of the leading edge from the maximum camber point

B flow blockage

c blade chord

c_a full-blade axial length

$c_\%$ tip clearance/mean blade height ratio $c_\% = \delta/h_m$

D diameter, diffusion factor

D_{ch} hydraulic diameter of blade channels

$\boldsymbol{e}_\vartheta$ unit vector in azimuthal direction

f friction coefficient

h specific enthalpy

h_m mean blade height

L axial length

L_{ch} effective length of blade channels

L_{eq} equivalent duct length

M_c Carter's rule coefficient

$\dot{m}$ mass flow rate

N number of blades

p,p_t static and total pressures

P (local) blade pitch

Q volumetric flow rate

$\boldsymbol{r}$ position vector

r radial coordinate

Re Reynolds number $Re = 2\Omega r_T^2/v$

Re_δ tip clearance Reynolds number $Re_\delta = 2\Omega\delta r_T/v$

r_H inducer hub radius

r_M inducer mean radius

r_T inducer tip radius

s azimuthal blade spacing

T flow temperature

$\boldsymbol{u}$ flow velocity

u radial fto\v velocity

U freestream boundary layer velocity

v azimuthal flow velocity

V absolute value of the flow velocity

w axial flow velocity

z axial coordinate

Greek Symbols

β_b blade angle evaluated w.r.t. the azimuthal direction

β'_2 relative discharge flow angle without deviation

γ	blade angle from axial direction
δ	boundary layer thickness, blade tip clearance
δ^*	boundary layer displacement thickness
δ°	discharge flow deviation angle
ϑ	azimuthal coordinate
θ^*	boundary layer momentum thickness
ρ	flow density
ν	kinematic viscosity
σ	blade solidity, cavitation no. $\Phi=\left(p_1-p_v\right)/\frac{1}{2}\rho\Omega^2 r_T^3$
Φ	flow coefficient, $\Phi=Q/\pi\Omega r_T^3$
Ψ	slip velocity stream function
Ψ	static head coefficients $\Psi=\left(p_2-p_1\right)/\frac{1}{2}\rho\Omega^2 r_T^2$
Ψ_t	total head coefficients $\Psi_t=\left(p_{t2}-p_{t1}\right)/\frac{1}{2}\rho\Omega^2 r_T^2$
Ω	inducer rotational speed
$\boldsymbol{\Omega}$	inducer rotational speed (vector)

Special Notations

q'	value of q in the rotating frame
$\bar{q}$	mean value of q

$\hat{\boldsymbol{u}}$	fully-guided flow velocity
$\tilde{\boldsymbol{u}}$	slip flow velocity

Subscripts

D	design conditions
T	tip radius
h	high clearance
H	hub radius
l	low clearance
le	leading edge
te	trailing edge
δ°	flow deviation angle
1	upstream station
2	downstream station

Acronyms

BVP	Boundary Value Problem
CPRTF	Cavitating Pump Rotordynamic Test Facility
ODE	Ordinary Differential Equation
2D	two-dimensional
3D	three-dimensional

1 Introduction

Current rocket propellant feed turbopumps often employ an inducer upstream of the centrifugal stage in order to avoid unacceptable cavitation, improve the suction performance and reduce the propellant tank pressure and weight. The main purpose of inducers consists in sufficiently pressurizing the flow for the main pump to operate satisfactorily. Compared to centrifugal pump impellers, typical inducers have fewer blades (usually 3 or 4), lower flow coefficients (from 0.05 to 0.1), larger stagger angles (70°to 85°) and significantly higher blade solidities (between 1.5 and 2.5). Long blades with small angles of attack provide ample time and room for the collapse of the cavitation bubbles and for the gradual exchange of energy with the flow. The resulting configuration, even though beneficial from the standpoint of cavitation performance, results in relatively low values of the inducer efficiency due to the highly viscous, turbulent and dissipative flow inside the blade passages.

The development of three-dimensional (3D) theoretical models capable of rapidly predicting the performance of axial inducers in order to provide indications for the preliminary design of the machine is of particular interest to rocket engineers. However, not many such models have been proposed so far, probably due to the difficulty of adequately describing the 3D flow field inside the inducer blades. Therefore, designers often refer to simple "rules of thumb" or to the general indications of design manuals such as the one published NASA (Jakobsen, 1971)[1]. In the past decades, numerical simulation of the complex 3D features of inducer flows has emerged as a promising tool for design validation and refinement (see, for example, Ashihara et al., 2002; Kang et al., 2007)[2-3], but its use in the stages of design still remains impractical.

A number of two-dimensional models for the prediction

of the noncavitating flow in turbopump inducers have been illustrated by Brennen, 1994, 1995[4-5]. These models are based on linear and radial cascade analyses with semi-empirical inclusion of flow deviation and viscous effects. Three-dimensional corrections for inlet flow prerotation, leakage, and discharge flow are also indicated. More recently Lakshminarayana, 1982[6], addressed the problem of performance prediction of noncavitating inducers by the combined use of a simplified radial equilibrium and the Euler equation. Viscous effects are taken into account through an empirical loss coefficient deduced from the reported performance of inducers documented in the literature. Indications on the effects of solidity and number of blades are also provided.

A second class of models has been aimed at the prediction of the effects of cavitation on inducer performance (Stripling and Acosta, 1962; Cooper, 1967; Brennen and Acosta, 1973; Brennen, 1978)[7-10]. Also these models are essentially two dimensional, where cavitation is assimilated to a vapor layer on the blade or a mixture of bubbles and liquid. Early studies opened the way to a number of more recent analyses capable of better understanding and predicting the major flow instabilities affecting cavitating inducers (see, for instance, Tsujimoto et al., 1993, 1998; Watanabe et al., 1999; Semenov et al., 2004; Pasini et al., 2011)[11-15].

In 2007, Bramanti et al., 2007[16], developed a simplified model based on the traditional throughflow theory approximations with empirical corrections for incidence, friction, and deviation losses of the flow through the inducer blades. The model proved to be in good agreement with the reported performance of several inducers tested in different facilities worldwide.

Expanding on this exploratory work, d'Agostino et al., 2008a, 2008b, 2008c[17-19], developed and successfully tested a quasi-3D reduced-order model for the preliminary geometric definition and noncavitating performance predic-

tion of tapered axial inducers, whose results have been later extended by means of the similarity experiments by Torre et al., 2009[20], to account for tip leakage effects. The present invited lecture illustrates and summarizes the main features and results of these investigations. Later analyses by Cervone et al., 2012[21], also investigated the effects of the leading edge shape on the performance of helical inducers. Extension of the present model to the simultaneous geometry definition and performance prediction of centrifugal turbopumps has recently been carried out and validated by d'Agostino et al., 2012, 2017a, 2017b[22-24].

Under the assumptions of incompressible, inviscid and irrotational flow, the 3D velocity field inside the blade channels has been approximated as the superposition of a 2D cross-sectional vorticity correction on a fully-guided axisymmetric flow with radially uniform axial velocity. Suitable redefinition of the diffusion factor to bladings with non-negligible radial flow allowed for integral control of the blade loading and for the estimate of the boundary layer blockage at the specified design flow coefficient, providing a simple way to better match the hub profile with the axial variation of the blade angle in variable-pitch tapered inducers. Carter's rule has been used to account for flow deviation at the inducer trailing edge. Mass continuity, angular momentum conservation and the Euler equation have been used to propagate the solution downstream and derive a simple 2nd order boundary value problem (BVP), whose numerical solution determined the steady, axisymmetric, axial flow at the inducer discharge. Finally, the non-cavitating pumping performance has been obtained by correcting the Euler head by means of suitable correlations for turbulence losses, flow incidence and deviation. The model has been validated by comparing its results with the experimental data obtained in the Cavitating Pump Rotordynamic Test Facility (CPRTF) for some space rocket inducers of European design and with the reported performance of a number of inducers tested in Japanese laboratories (Cervone et al., 2005, 2006, 2007)[25-27]. Head correction for tip leakage effects has been carried out based on the results of the similarity experiments by Torre et al., 2009 [20], on a three-bladed inducer designed according to the indications of the present model. Comparison of the pumping performance and geometry a number of high-head inducers documented in the literature confirmed the validity and accuracy of the proposed midel.

2 Inducer Flow and Geometry

2.1 Flow Velocity

The incompressible, inviscid, irrotational flow through a helical inducer with N radial blades, rotational speed Ω, constant tip radius r_T, tapered-hub radius r_H, variable axial pitch P, and blade angle γ (as schematically shown in Fig. 1) is held by the equations:

$$\nabla \cdot \boldsymbol{u} = 0$$
$$\nabla \times \boldsymbol{u} = 0$$

The relatively large value of the blade solidity typical of inducers designed for controlling cavitation in highly loaded turbopumps suggests that near design conditions ($\Phi \cong \Phi_D$),

the 3D velocity $\boldsymbol{u}$ the blade channels can be approximated by the superposition of a guided axisymmetric flow a with radially uniform axial velocity component $\widehat{w}$ and a 2D cross-sectional slip velocity correction (Fig. 2):

$$\boldsymbol{u} = \widehat{\boldsymbol{u}} + \widetilde{\boldsymbol{u}}$$

With reference to the velocity triangles of Fig. 3, for radial helical blades:

$$\tan\gamma = \frac{2\pi r}{P} \begin{cases} \widehat{v} = [\Omega r - \widehat{w}\tan\gamma = \Omega r - 2\pi r\dfrac{\widehat{w}}{P}] \\ \widehat{w} = \dfrac{\dot{m}}{\rho\pi\left(r_T^2 - r_H^2\right)B} = \dfrac{\Phi\Omega R_T^3}{\left(r_T^2 - r_H^2\right)B} \end{cases}$$

where $0 \le B \le 1$ is the average cross-sectional blockage due to the boundary layer displacement effects and, if significant, to blade thickness. The 2D slip velocity components are most synthetically expressed and solved for in terms of a scalar stream function $\Psi(r', \vartheta')$ in the rotating cylindrical coordinates $r' = r, \vartheta' = \vartheta - \Omega t$, and $z' = z$:

$$\widetilde{u} = \frac{1}{r'}\frac{\partial\Psi}{\partial\vartheta'} \text{ and } \widetilde{v} = \frac{\partial\Psi}{\partial r'}$$
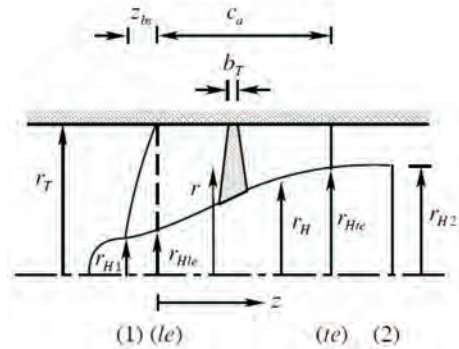

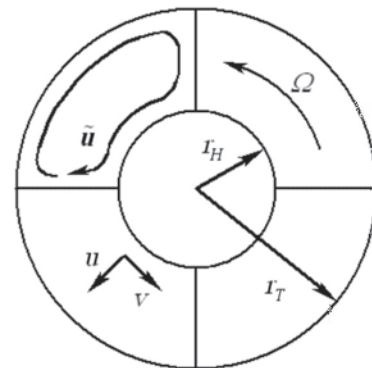Fig.1 Inducer schematic and nomenclature

Fig.2 Schematic of the 2D cross-sectional slip velocity correction in the inducer blade channels
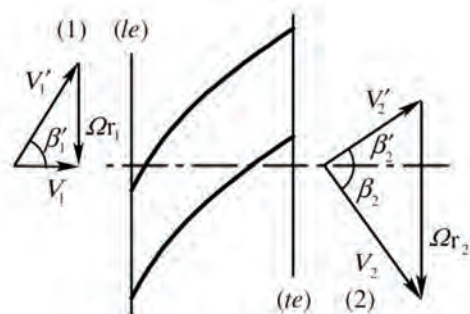

Fig.3 Velocity triangles

2.2 Inducer Tip and Hub Radii

Substitution of the assumed velocity field in the expressions of the incompressibility and irrotationality conditions in cylindrical coordinates r, ϑ, z yields:

$$\frac{\partial(r\hat{u})}{\partial r} = -r\frac{d\hat{w}}{dz}$$

$$\frac{d}{dz}\left(\frac{\hat{w}}{P}\right) = 0$$

$$\frac{d^2\hat{w}}{dz^2} = 0$$

$$\frac{1}{r}\frac{\partial}{\partial r}\left(r\frac{\partial\Psi}{\partial r}\right) + \frac{1}{r'^2}\frac{\partial^2\Psi}{\partial\vartheta'^2} = 2\Omega - 4\pi\frac{\hat{w}}{P}$$

Integration of $d^2\hat{w}/dz^2 = 0$ with the boundary conditions $\hat{w}(0) = \hat{w}_{le}$ and $\hat{w}(c_a) = \hat{w}_{te}$ at the axial locations bounding the full-height portion of the blades (indices le and te) yields:

$$\frac{d\hat{w}}{dz} = \frac{\hat{w}_{te} - \hat{w}_{le}}{c_a} \equiv const$$

and the following expression for the axial velocity:

$$\hat{w} = \hat{w}_{le}(\hat{w}_{te} - \hat{w}_{le})\frac{z}{c_a}$$

Similarly, integrating the continuity equation with the impermeability condition $\hat{u}(r_\tau) = 0$ at the tip radius, the following expression for the radial velocity is obtained:

$$\hat{u} = \frac{1}{2}\frac{d\hat{w}}{dz}\left(\frac{r_t^2}{r} - r\right)$$

Finally, evaluating $\hat{w}$ at design conditions (index D) by means of the continuity equation and integrating $d = (\hat{w}/P)dz = 0$ with $P(\hat{w}_{leD}) = P_{Tle}$ at $z = 0$, the following expressions for matching the axial changes of the hub radius r_H and blade pitch P are obtained:

$$\frac{1}{(r_T^2 - r_H^2)B} = \frac{1}{(r_T^2 - r_H^2)B_{le}} + \left[\frac{1}{(r_T^2 - r_{Hle}^2)B_{le}} - \frac{1}{(r_T^2 - r_{Hle}^2)B_{le}}\right]\frac{z}{c_a}$$

$$P = P_{Tle}\frac{\hat{w}_D}{\hat{w}_{leD}} = P_{Tle} + P'z$$

where:

$$P' = B_{le}(B_{te} - B_{le})\frac{z}{c_a}$$

and a linear axial variation of the blockage can be approximately assumed inside the blade passages from the leading edge station (le), where $B = B_{le} \cong 1$, to the trailing edge (te) where $B = B_{te}$. The assumption of no leading edge blockage implies zero blade thickness, no leading edge separation, and zero initial boundary thickness. Given the relative magnitudes of blade and boundary layer thicknesses and the level of accuracy of the present model, these effects can be considered of second order and therefore have not been taken into account.

2.3 Slip Flow

Finally, on each channel cross section, Poisson's equation for the stream function can be conformally mapped in a rectangular domain and integrated standard methods (Hildebrand, 1976)[28] with the condition $\Psi = 0$ on the boundary to:

$$\Psi = -\sum_{m=1}^{+\infty}-\sum_{n=1}^{+\infty}C_{m,n}\sin\left[m\pi\frac{ln(r/r_H)}{ln(r_T/r_H)}\right]\sin\frac{(2n-1)N\vartheta'}{2}$$

where:

$$C_{m,n} = \frac{A_{m,n}}{m^2\pi^2/ln^2(r_\tau/r_H) + (n - \frac{1}{2})^2N^2}$$

$$A_{m,n} = Kr_H^2\frac{m/(n - \frac{1}{2})ln^2(r_T/r_H)}{1 + m^2\pi^2/4ln^2(r_T/r_H)}\left[-1 - (-1)^m\frac{r_H^2}{r_T^2}\right]$$

and

$$K = 2\Omega - 4\pi\frac{\hat{w}}{P} = 2\Omega\left[1 - \frac{2\pi\Phi r_T^3}{P(r_T^2 - r_H^2)}\right]$$

from which the radial and tangential slip velocity components $\hat{u}$ and $\hat{v}$ are readily computed.

2.4 Blade Loading and Boundary Layer Blockage

With reference to Fig. 4, suitable redefinition of the diffusion factor for axial bladings (Lieblein et al., 1953)[29]:

$$D = \frac{V_1' - V_2'}{V_1'} + \frac{(v_2 - v_1)}{2\sigma V_1'} \cong \frac{p_2 - p_1}{\frac{1}{2}\rho V_1'(V_1' + V_2')} + \frac{p_{t2} - p_{t1}}{\sigma\rho\Omega(r_1 + r_2)V_1'}$$

to the case of tapered inducers with non-negligible radial flow allows for the control of the blade loading (a crucial design aspect under cavitating conditions) and the estimate of the boundary blockage at nominal flow conditions.

By evaluating:

$$p_2 - p_1 = \frac{1}{2}(V_1^2 - V_2^2) - \frac{1}{2}\rho\Omega^2(r_1^2 - r_2^2)$$

$$p_{t2} - p_{t1} = \rho\Omega(r_2v_2 - r_1v_1)$$

with Bernoulli's and Euler's equations for mixed-flow bladings and substituting in the above expression for D obtain:

$$D \cong \frac{V_1' - V_2'}{V_1'} - \frac{\Omega^2(r_1^2 - r_2^2)}{V_1'(V_1' + V_2')} + \frac{r_2v_2 - r_1v_1}{\sigma(r_1 + r_2)V_1'}$$
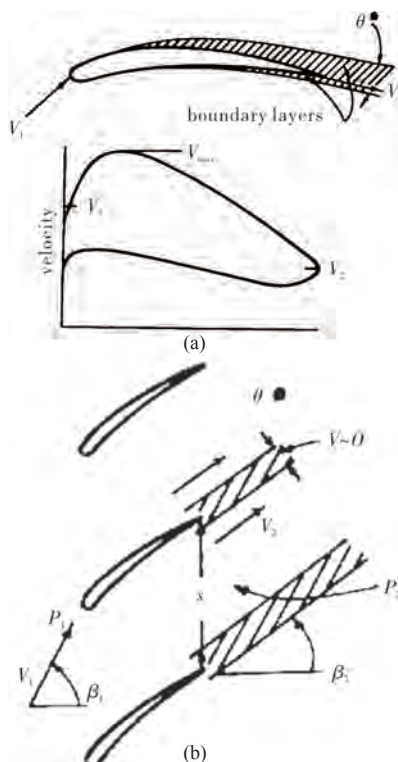

(a)

(b)

Fig.4 Nomenclature for blade boundary layer (a) and linear cascade (b).

Here all relevant properties including the solidity $\sigma = c/s$ are evaluated on the mean streamline:

$$r = r_M = \sqrt{\frac{r_T^2 + r_H^2}{2}}$$

and, for flow with no inlet prerotation and fully guided at the inducer outlet ($v_1 \cong 0$ and $v_2' \cong w_{te}\tan\gamma_{te}$) the relative velocities are expressed by:

$$v_1' = \sqrt{w_1^2 + V_1'^2} = \sqrt{(\frac{\Phi\Omega r_T^3}{r_T^2 - r_{Hle}^2})^2 + \Omega^2 r^2}$$

$$v_2' = \sqrt{w_2^2 + V_2'^2} \cong \frac{\Phi_D\Omega r_T^3}{(r_T^2 - r_{H2}^2)\cos\gamma_{te}}$$

As illustrated in Fig. 5, in turbulent boundary over blade cascades) the diffusion factor is correlated with the momentum thickness θ^* (Lieblein, 1965; Brennen, 1994)[30,4]:
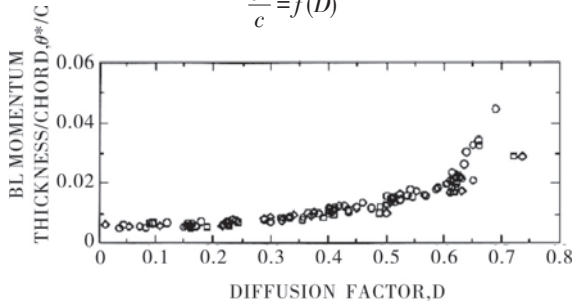
$$\frac{\theta^*}{c} = f(D)$$

Fig.5 Ratio of the momentum thickness ϑ^* of the blade boundary layer to the chord c as a function of the diffusion factor D, for axial cascades with three different profiles (adapted from Brennen (1994))[4].

Furthermore, by using the Prandtl equations for the turbulent boundary velocity profile on a fiat plate (Prandtl and Tietjens, 1934; White, 1974)[31-32], it is possible to show that the displacement thickness is $\delta^* \cong 1.3\theta^*$. With these results, the blade boundary layer blockage at the inducer edge is computed as:

$$B_{te} = 1 - \frac{2\delta^*}{S_{te}\cos\Psi_{te}}$$

(Fig. 4) where the blade spacing $S_{te} = 2\pi r_{te}/N$ is evaluated at the mean radius.

2.5　Mean Radius, Chord, and Solidity

On a relative streamline of the guided flow:

$$\frac{\mathrm{d}r}{\hat{u}'} = \frac{r\mathrm{d}\vartheta'}{\hat{v}'} = \frac{\mathrm{d}z}{\hat{w}'}$$

where from earlier results:

$$\hat{u}' = \hat{u} = \frac{1}{2}P'\frac{\hat{w}_{le}}{P_{Tle}}(\frac{r_T^2}{r} - r)$$

$$\hat{v}' = \Omega r - \hat{v} = 2\pi r\frac{\hat{w}_{le}}{P_{Tle}}$$

$$\hat{w}' = \hat{w} = \frac{\hat{w}_{le}}{P_{Tle}}(P_{Tle} + P'z)$$

Hence, integrating with initial conditions r_{Mle}, ϑ'_{Mle}, z_{Mle}, the equations of the mean streamline are:

$$r_M = \sqrt{r_T^2 - (r_T^2 - r_{le}^2)\frac{P_{Tle} + P'z_{Mle}}{P_{Tle} + P'z_M}}$$

$$\vartheta'_M = \vartheta'_{Mle} + \frac{2\pi}{P'}\ln\frac{P_{Tle} + P'z_M}{P_{Tle} + P'z_{Mle}}$$

The mean values of the blade chord and are then evaluated as:

$$c = \int_{z_{Mle}}^{z_{Mle} + c_a} \mathrm{d}z_M \sqrt{\left(\frac{\partial r_M}{\partial z_M}\right)^2 + \left(r_M\frac{\partial\vartheta'_M}{\partial z_M}\right)^2 + 1}$$

$$\sigma = \int_{z_{Mle}}^{z_{Mle} + c_a}\frac{\mathrm{d}c}{S_M} = \int_{z_{Mle}}^{z_{Mle} + c_a}\frac{\mathrm{d}z_M}{2\pi r_M/N}\sqrt{\left(\frac{\partial r_M}{\partial z_M}\right)^2 + \left(r_M\frac{\partial\vartheta'_M}{\partial z_M}\right)^2 + 1}$$

2.6　Flow Pressure in the Blade Channels

The pressure of the (absolutely) irrotational flow in the blade channels can readily be obtained by straightforward integration of steady Bernoulli's equation in the reference frame r, ϑ', z rotating with the inducer:

$$\nabla\left(\frac{p}{\rho} + \frac{1}{2}\boldsymbol{u}'\cdot\boldsymbol{u}' - \frac{1}{2}\Omega^2\boldsymbol{r}\cdot\boldsymbol{r}\right) = \boldsymbol{u}'\times(\nabla\times\boldsymbol{u}) = 0$$

where the same integration constant:

$$C = p_1 + \frac{1}{2}\rho w_1^2$$

applies over the entire flow field, and the velocity $\boldsymbol{u}'$ is expressed by:

$$\boldsymbol{u}' = \boldsymbol{u} - \Omega\times r = \boldsymbol{u} - \Omega r e_\vartheta$$

Therefore, with earlier notations:

$$\boldsymbol{u}'\cdot\boldsymbol{u}' = (\hat{u} + \tilde{u})^2 + (\hat{v} + \tilde{v} - \Omega r)^2 + \hat{w}^2$$

and, solving for the flow pressure 2.t the generic location in the blade channels:

$$p_1 + \frac{1}{2}\rho\left[w_1^2 - (\hat{u} + \tilde{u})^2 - (\hat{v} + \tilde{v})^2 + 2(\hat{v} + \tilde{v})\Omega r - \hat{w}^2\right]$$

3　Inducer Performance

3.1　Discharge Flow

No inlet flow prerotation is assumed, thus implicitly referring for the application of Euler to a control volume extending· in the upstream direction down to the region of unswirled flow in the inducer suction line. This approach neglects the torque of shear forces on the inner surfaces of the inlet line and therefore in the present inviscid flow approximation correctly estimates the power exerted by the inducer on the flow.

In the assumption of uniform inlet flow to the inducer with no prerotation ($v_1 = 0$) radial differentiation of the incompressible isentropic Euler equation:

$$\frac{p_2}{\rho} + \frac{1}{2}(v_2^2 + w_2^2) - \frac{p_1}{\rho} - \frac{1}{2}(v_1^2 + w_1^2) = \Omega(r_2v_2 - r_1v_1)$$

for the axisymmetric flow at sections (1) and (2) of Fig. 1 and elimination of the pressure by means of the radial equilibrium condition:

$$\frac{v^2}{r} = \frac{1}{\rho}\frac{\partial p}{\partial r}$$

yields the following ODE for the axial and tangential velocity profiles $w_2(r_2)$ and $v_2(r_2)$ at the

inducer discharge section:

$$\frac{1}{2}\frac{\mathrm{d}^2 w_2^2}{\mathrm{d}r_2} + \left(\frac{v_2}{r_2} - \Omega\right)\frac{\mathrm{d}(r_2v_2)}{\mathrm{d}r_2} = 0$$

In order to solve the above equation for the axial velocity profile it is necessary to establish a correlation between w_2 and the azimuthal velocity v_2. To this purpose the fully-guided flow with uniform axial velocity and slip vorticity correc-

tion at the inducer trailing edge (station te):

$$u_{te} = \tilde{u}_{te}$$

$$v_{te} = \Omega r_{te} - w_{te}\frac{r_{te}}{r_T}\tan\gamma_{Tle} + \tilde{v}_{te}$$

$$w_{te} = \frac{\Phi\Omega r_T^2}{r_T^2 - r_{Hle}^2}$$

is assumed to mix into an axisymmetric swirled axial flow with velocities v_2 and w_2 at the discharge section (station 2), while satisfying mass continuity and, in the absence of wall friction, conserving the axial component of angular momentum:

$$2\pi v_2 r_2 \mathrm{d}r_2 = 2\pi v_{te} r_{te}\mathrm{d}r_{te}$$

$$2\pi w_2 v_2 r_2^2 \mathrm{d}r_2 = 2\pi w_{te} r_{te}^2 \mathrm{d}r_{te}\int_0^{2\pi} v_{te}\mathrm{d}\vartheta'$$

Integration of the second equation with earlier expressions of v_{te} and $\tilde{v}_{te}$ yields:

$$v_2 = \frac{r_{te}}{r_2}\left[\Omega r_{te} - w_{te}\frac{r_{te}}{r_T}\tan\gamma_{Tle} + \tilde{v}_s(r_{te})\right]$$

where:

$$\tilde{v}_s(r_{te}) = \frac{1}{r_{te}}\sum_{m=1}^{+\infty}\sum_{n=1}^{+\infty}\frac{mC_{m,n}}{(n-\frac{1}{2})\ln(r_T/r_H)}\cos\left[m\pi\frac{\ln(r_{te}/r_{Hle})}{\ln(r_T/r_H)}\right]$$

Finally, substitution in the ODE for the axial velocity profile where, from the mass balance:

$$\frac{d}{dr_2} = \frac{dr_{te}}{dr_2}\frac{d}{dr_{te}} = \frac{w_2 r_2}{w_{te}r_{te}}\frac{d}{dr_{te}} \text{ and } \frac{dr_{tre}^2}{dr_2^2} = \frac{w_2}{w_{te}}$$

results in the following BVP (boundary value problem) for w_2 and r_{te} as functions of r_2^2:

$$\frac{dw_2}{dr_2^2} = \frac{1}{2w_{te}}\left[\Omega - \left(\Omega - \frac{w_{te}}{r_T}\tan\gamma_{Tte} + \frac{\tilde{v}_s(r_{te})}{r_{te}}\right)\frac{r_{te}^2}{r_2^2}\right]\times$$

$$\left\{2\Omega - 2\frac{w_{te}}{r_T}\tan\gamma_{Tte} + \frac{1}{r_{te}}\frac{d}{dr_{te}}\left[r_{te}\tilde{v}_s(r_{te})\right]\right\}$$

$$\frac{\mathrm{d}r_{tre}^2}{\mathrm{d}r_2^2} = \frac{w_2}{w_{te}}$$

The above problem can then be solved by numerical shooting from r_{H2}^2 to r_T^2 with initial conditions:

$$w_2(r_{H2}^2) = w_{H2} \text{ and } r_{te}^2(r_{H2}^2) = r_{Hte}^2$$

iterating on the assumed value of w_{H2} until the final boundary condition $r_{te}^2(r_T^2) = r_T^2$ is satisfied. A closed form approximation of the axial velocity profile $w_2(r_2)$ can also be obtained by assuming $r_{te} \cong r_2$ in the expression of v_2 and neglecting $\tilde{v}_s$ in:

$$\frac{v_2}{r_2} - \Omega = -\frac{w_2}{r_T}\tan\gamma_{T2} + \frac{\tilde{v}_s}{r_2} \cong -\frac{v_2}{r_2}\tan\gamma_{T2}$$

Then the ODE for the axial velocity profile becomes:

$$\frac{\mathrm{d}w_2}{\mathrm{d}r_2} - \frac{1}{r_T}\tan\gamma_{T2}\frac{\mathrm{d}(r_2 v_2)}{\mathrm{d}r_2} = 0$$

whose solution is:

$$w_2(r_2) = \frac{\left[\Omega r_2 + \tilde{v}_s(r_2)\right](r_2/r_T)\tan\gamma_{T2} + c}{1 + (r_2^2/r_T^2)\tan\gamma_{T2}}$$

with the integration constant c determined by the mass balance between the inlet and discharge cross-sections:

$$\int_{r_{H2}}^{r_T} w_2 2\pi r_2 dr_2 = \int_{r_{H1}}^{r_T} w_1 2\pi r_1 dr_1$$

3.2 Flow Losses

The assumptions of inviscid and fully-guided flow at the inducer trailing edge are not accurately satisfied in practice. In order to better approximate the actual pumping characteristic of noncavitating inducers the main sources of performance degradation (flow incidence, friction and deviation) have to be accounted for.

Friction losses in the blade channels are evaluated by means of standard correlations for turbulent duct flows

$$\Delta p_{friction} = f\frac{L_{ch}}{D_{ch}}\frac{1}{2}\rho V_1^{'2}$$

where the friction factor f depends on the Reynolds number based on the hydraulic diameter D_{ch} of the blade channels, L_{ch} is the effective channel length evaluated along the mean-streamline, and $V_1^{'}$ is the relative flow velocity at the mean inlet radius.

Incidence losses due to the sudden change of the flow direction at the leading edge of the inducer blades are expressed in terms of a nondimensional equivalent length L_{eq}/D_{ch}, function of the incidence angle evaluated on the mean streamline. Hence, the overall pressure losses can be written as follows:

$$\Delta p_{loss} = f\left(\frac{L_{ch}}{D_{ch}} + \frac{L_{eq}}{D_{ch}}\right)\frac{1}{2}\rho V_1^{'2}$$

Finally, the mean value of the exit flow deviation is evaluated at the mean radius using Carter's correlation:

$$\delta° = \frac{m_c}{\sqrt{\sigma}}(\gamma_{le} - \gamma_{te})$$

and applied to correct the discharge flow direction at all radii in the inducer annulus. In order to better match the experimental data, the standard correlation for the coefficient m_c has been slightly modified according to the equation:

$$m_c = 1.22\left[0.23\left(\frac{2a}{c}\right)^2 + 0.1\left(\frac{\gamma_{te}}{50°}\right)\right]$$

where $a \cong c/2$ is the relative position of the maximum camber point from the blade leading edge. Hence, the azimuthal flow velocity at the inducer discharge section (2) with flow deviation corrections becomes:

$$v_{2\delta°} = \Omega r - w_2\tan(\beta_2' + \delta°)$$

where:

$$\beta_2' = \tan^{-1}\left(\frac{\Omega r - v_2}{w_2}\right)$$

3.3 Pumping Performance

With the above results, the baseline pumping performance in the absence of tip clearance losses is readily evaluated from the Euler equation:

$$\frac{p_{t2} - p_{t1}}{\rho} = \frac{p_2 - p_1}{\rho} + \frac{v_{2\delta°}^2 + w_2^2 - w_1^2}{2} = \Omega r_2 v_{2\delta°} - \frac{\Delta p_{loss}}{\rho}$$

Hence, by mass averaging the pressure changes, the total and static head coefficients are expressed by:

$$\Psi_t = \frac{1}{\Omega^2 r_T^2 \dot{m}}\int_{r_{H2}}^{r_T}(p_{t2} - p_{t1})w_2 2\pi r_2 dr_2$$

$$\Psi = \frac{1}{\Omega^2 r_T^2 \dot{m}}\int_{r_{H2}}^{r_T}(p_2 - p_1)w_2 2\pi r_2 dr_2$$

3.4 Tip Clearance Losses

The effects of blade tip clearance and Reynolds scaling on the pumping performance of high-head helical inducers has been characterized in a test campaign conducted in the

CPRTF on a three-bladed, tapered-hub, variable-pitch inducer (see Figure 6) named DAPAMITO3. The test inducer, whose main geometrical and operational parameters are reported in Table 1, is made in 7075-T6 aluminum alloy and has been designed in accordance with the indications of the present model.
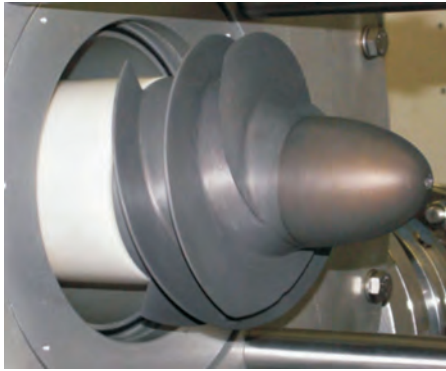

Fig.6　The DAPAMITO3 inducer without the Plexiglas inlet pipe

The overall dimensions of this inducer have been chosen for easy installation and testing in the current CPRTF configuration. A moderate value of the blade loading (with a diffusion factor $D = 0.39$) and a high solidity ($\sigma_T = 2.03$) have been chosen for reducing the leading-edge cavity and improving the suction performance. The value of the tip incidence-to-blade angle ratio $\alpha/\beta_b < 0.5$ has been selected with the aim of controlling the danger of surge instabilities at design flow under cavitating conditions.

Tab.1　Geometrical and operational parameters of the DAPAMITO3 inducer.

Design flow coefficient	–	Φ_D	0.059
Number of blades	–	N	3
Tip radius	mm	r_T	81
Inlet tip blade angle	deg	γ_{Tle}	83.1
Inlet hub radius(fully−developed blade)	mm	r_{Hle}	44.5
Outlet hub radius	mm	r_{Hte}	58.5
Mean blade height	mm	h_m	29.5
A xial length(fully−developed blade)	mm	c_a	63.5
Rotational speed	rpm	Ω	3 000
Inlet hub radius	mm	r_{Hl}	35
A xial length	mm	L	90
Diffusion factor	–	D	0.39
Ratio between tip incidence and blade angles	–	α/β_b	0.30
Tip solidity	–	σ_T	2.03
Incidence tip angle@design	deg	α	2.07
Outlet tip blade angle	deg	γ_{Te}	74.58

The tests on the DAPAMITO3 inducer reported in the present paper have been carried out in the Cavitating Pump Rotordynamic Test Facility (CPRTF), specifically designed for characterizing the performance of cavitating/non-cavitating turbopumps in a wide variety of alternative configurations (axial, radial or mixed flow, with or without an inducer; Rapposelli et al., 2002a, 2002b; Pace et al., 2012)[33-35]. The facility operates in water at temperatures up to 90 °C and is intended as a flexible apparatus readily adaptable to conduct experimental investigations on virtually any kind of fluid dynamic phenomena relevant to high performance turbopumps. The test section can be equipped with a rotating dynamometer, for the measurement of the forces and moments acting on the impeller, and with a mechanism for adjusting and rotating the eccentricity of the impeller axis in the range 0÷2 mm and ±3000 rpm. The inlet section, made in Plexiglas, is transparent in order to allow for the optical visualization of the cavitation on the test inducer. It can be easily replaced, allowing for testing inducers with different tip diameters and clearances.

For the present experimental work the facility has been assembled in a simplified configuration without the rotating dynamometer. The inlet pressure and the pressure rise, necessary for the characterization of the pump performance, have been measured by means of an absolute pressure transducer (Druck, model PMP 1 400, 0÷1.5 bar, 0.25% precision), installed about one inducer diameter upstream of the leading edge cross-section, and a differential pressure transducer (Kulite, model BMD 1P 1 500 100, range 0-6.9 bard, 0.1% precision), installed between the inlet and the outlet sections of the test pump (with the low pressure tap at the same location as the absolute pressure tap and the high pressure tap one inducer diameter downstream of the trailing edge cross-section). Two electromagnetic flowmeters (mod. 8732C by Fisher-Rosemount, range 0-100 l/s, 0.5% precision), mounted on the suction and discharge lines, measure the pump's inlet/outlet flow rates and a resistance thermometer measures the working fluid temperature with ±0.5 K precision.

The DAPAMITO3 inducer has been mounted in the CPRTF using a Plexiglas casing designed for providing the same clearance/mean blade height ratio($c_\% = 2.7\%$) of the reference configuration used for setting the model. Each experimental point has been obtained averaging the differential pressure and flow rate signals acquired for 5 s at 200 sps. The rotational speed and the water temperature have been kept constant at 2 500 rpm (±3 rpm) and 19.2 °C (±1℃) respectively, in order to attain fully-developed turbulent operation ($Re = 2\Omega r_T^2/v = 3.32 \cdot 10^6$).
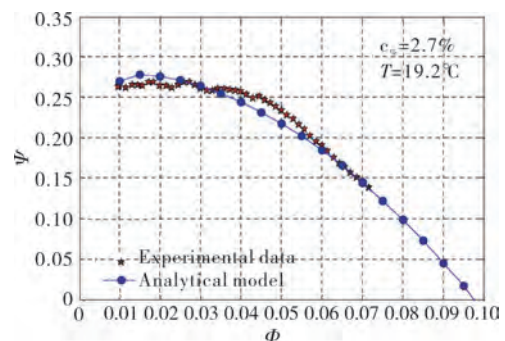

Fig.7　Comparison between the experimental and analytically predicted non-cavitating performance of the DAPAMITO 3 inducer ($\Omega = 2\,500\,\text{rpm}$, $Re = 3.32 \times 10^6$).

Figure 7 reports the experimental pumping performance (red stars) compared to the results obtained from the analytical model (blue circles). The close agreement of the two data sets confirms both the predictive capability of the reduced order model and the high-bead nature ($\Psi > 0.15$), as reported in Jakobsen, 1971)[1] of the DAP AMITO3 inducer. Efforts have been directed to generalizing the predictions of the analytical model in order to account for clearance variations. As reported in the literature (Brennen, 1994) [4], the performance of non-cavitating inducers is relatively insensitive to the clearance for $c_\% < 2\%$ and declines rapidly for larger values of $c_\%$. Clearance changes affect both the inducer bead and the flow coefficient, which are modified by the backflow. The relationship between the variations of the bead and flow coefficients can be obtained by assuming that the hydrodynamic nature of the test rig losses is not influenced by changes of the inducer tip clearance, all other operational conditions being the same (see the schematic representation in Figure 8).

Under this assumption, the relation between the bead and the flow coefficients at different clearances becomes:

$$\Phi_l = \Phi_h \sqrt{\frac{\Psi_l}{\Psi_h}}$$

where the subscripts l and h refer to different clearances, one lower (l) than the other (h). This equation allows for the non-cavitating inducer performance to be scaled for different tip clearances once the associated head change is known. On the basis of this simple correlation, the model has been modified to take in to account the actual clearance/mean blade height ratio.

Figure 9 reports the effect of tip clearance on the non-cavitating performance of an inducer adapted from Brennen, 1995[5]: the head coefficient bas been made non-dimensional using the head coefficient (Ψ_0) corresponding to a clearance/blade height ratio of 1.12%, where the clearance effect seems to invert its trend. The empirical correlation reported in Figure 9 can be used for estimating the ratio Ψ_l/Ψ_h and the previous equation gives the corresponding correction in terms of flow coefficients ratio.

Another series of cold water tests has been carried out on the DAPAMITO3 inducer aimed at experimentally validating the results of the proposed scaling for tip clearance effects. The inducer has been assembled in the CPRTF using a Plexiglas casing designed for providing a blade clearance-to-mean height ratio equal to 6.8%, a disproportionately large value sometimes used in the characterization of rotordynamic whirl forces to avoid rotor/stator contact. The non-cavitating performance curves have been obtained with the previous experimental procedure at constant water temperature (19.2 ± 1℃) using three different values of the rotational speed (1 500, 2 000 and 2 500 rpm, ± 3 rpm) in order to verify the Reynolds-independence of the test results.

Figure 10 reports the experimental pumping performance compared to the results predicted by the analytical model scaled for tip clearance effects (blue circles). The results confirm that the characteristic curves are Reynolds-independent, as expected since the flow is fully turbulent ($Re > 10^6$), and that the inducer head is reduced w.r.t. operation at the reference tip clearance value. The predicted performance curves are almost superposed to the experimental data, thus validating the effectiveness of the proposed method for tip clearance scaling.

3.5 Temperature Effects

The non-cavitating characteristic curve of the DAPAMITO3 inducer has been experimentally determined at different values of the temperature of the working fluid. As shown in Figure 11, the non-cavitating performance is affected by the variation of the water temperature. All tests have been conducted at fully-developed turbulent Reynolds numbers ($Re > 10^6$), and therefore at flow conditions where turbulence effects are Reynolds-independent. In present experiments the only relevant flow property that is significantly influenced by temperature is the kinematic viscosity, which for water decreases approximately by a factor of 3 from 20℃ to 75 ℃.
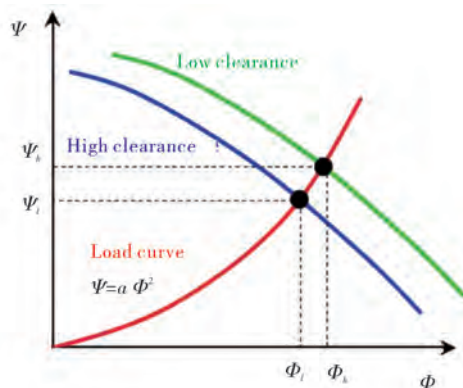
Fig.8 Schematic representation of two non-cavitating performance curves obtained with different tip clearance values (subscripts h and l refer to high and low clearances)
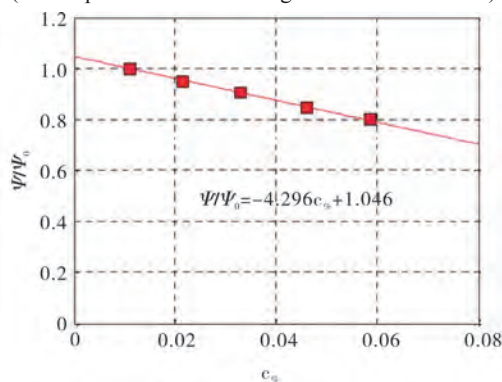
Fig.9 The effect of tip clearance on the non-cavitating performance (adapted from Brennen, 1995)[5]
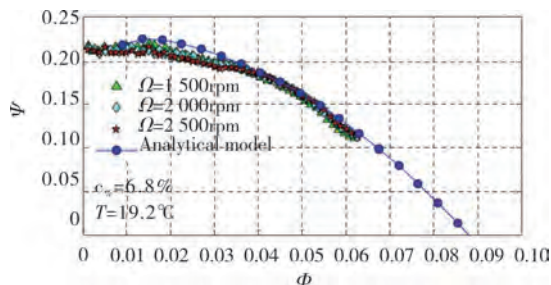
Fig.10 Comparison between the experimental and analytically predicted non-cavitating performance of the DAPAMITO3 inducer
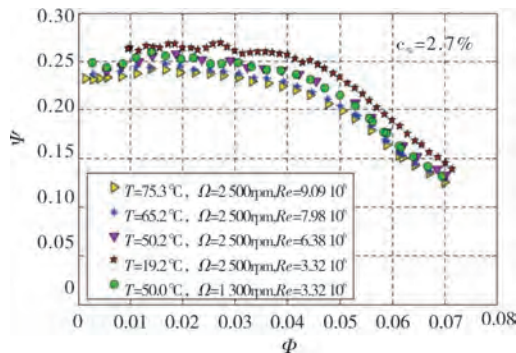
Fig.11 Non-cavitating performance of the DAPAMITO3 inducer at different water temperatures

The available evidence shows that the performance of the inducer decreases when the temperature of the flow is higher, and therefore its kinematic viscosity is lower. Furthermore, it is worth noting that even in the case of full Reynolds similarity, obtained by adjusting the rotational speeds to attain equal Reynolds numbers in both of the experiments, the characteristic curves obtained at different water temperatures do not overlap (red stars and green circles in Figure 11). On the other hand, two hot tests conducted at the same temperature essentially give the same characteristic curve even if the values of fully-developed turbulent Reynolds numbers are different (pink triangles and green circles in Figure 11). This result is fully consistent with the cold water tests carried out at the same temperature with different rotating speeds, illustrated in Figure 10.

As for the head degradation observed for different tip clearances, the reduction of the pumping performance of the inducer with the flow temperature is evident in the simultaneous decrease of both the head and flow coefficients along the load characteristics of the water loop, as expressed by the previous equation. It appears that the liquid temperature influences the intensity of the tip leakage. Strictly speaking, the temperature, which affects the physical properties of the working fluid, can also slightly modify the geometric similarity of the experiments when the rotor and stator have different thermal expansion coefficients. In particular, the thermal expansion coefficient of the Plexiglas casing is three times larger than that of the aluminum inducer. As a result of a preliminary analysis, this effect is not completely negligible, but it is not by itself sufficient to justify the degradation of the pumping performance experienced in the hot tests.

The available experimental evidence suggests therefore that the observed behavior of the head coefficient is due to the sensitivity of the tip clearance flow to the temperature of the working fluid. Viscous blockage effects reduce the tip leakage flow and their intensity is expected to scale with the tip clearance Reynolds number $Re_\delta = 2\Omega r_T \delta/v$, whose value is much lower than the value needed to attain Reynolds independence of the nondimensional inducer performance. Hence, changes of the tip clearance Reynolds number induced by the differential thermal expansion of rotor and stator are expected to affect the nondimensional performance of the inducer even at constant values of $Re = 2\Omega r_T^2/v$ in excess of 10^6.

Consistently with this interpretation, the results of Figure 12 confirm that the noncavitating performance of the DA-PAMITO3 inducer at different flow temperatures is well correlated to the tip clearance Reynolds number computed using the temperature- dependent liquid viscosity, neglecting the small changes of the tip clearance due to rotor/stator differential thermal expansion. The characteristic curve at 19.2℃ has been chosen as reference, while the ratio of the head coefficients has been extrapolated from the experimental data with the same scaling equation used for the clearance. In first approximation, the ratio between the head coefficients can be considered approximately linear v/s the tip clearance Reynolds number. The influence of the working fluid and its temperature on the non-cavitating performance is also evident in Yoshida et al., 2005[36], where the same test article has been tested in cold water and in liquid nitrogen. Due to the lower kinematic viscosity of the liquid nitrogen with respect to cold water, the non-cavitating head coefficient at the same flow coefficient is lower in nitrogen than in cold water.
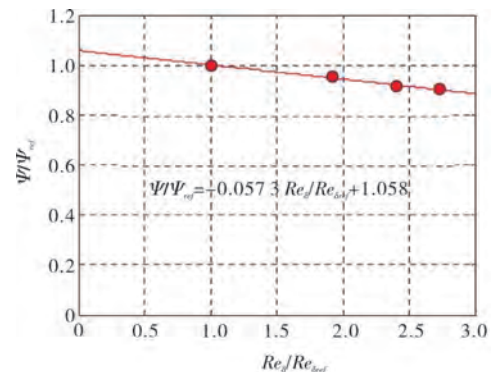

Fig.12 The effect of the tip clearance Reynolds number on the non-cavitating inducer performance.

4 Model Discussion and Validation

With reference to the definition of the inducer geometry, in the stated assumptions and approximations the standard requirement for radially uniform axial velocity in the blade channels at design conditions determines the correlation between the axial schedules of the hub radius and blade pitch angle of helical inducers. If, in particular, the hub-to-tip radius ratio is known at the leading and trailing edge sections and the design flow coefficient and leading edge blade angle are assigned, then all of the main geometric features of tapered hub helical inducers can be derived, including the trailing edge pitch angle. Comparison with the geometry of the MK1 and FAST2 space inducers, produced by Avio and tested in the Cavitating Pump Rotordynamic Test Facility (CPRTF), confirms that all of the main design characteristics and the relation between the hub geometry and the blade pitch are almost perfectly predicted by the proposed model.

As an example, Fig. 13 shows a three-dimensional drawing of a 4-bladed inducer designed by using the model. The inducer tip radius is 90.9 mm, the hub radius is 57 mm at the inlet and 73 mm at the outlet, the tip blade angle is 8.9 de-
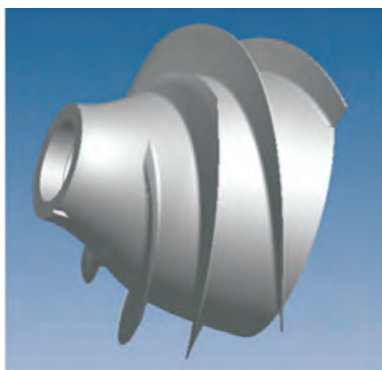
Fig.13   3D rendering of a four-bladed, tapered-hub, variable-pitch inducer designed according to the proposed model

Tab.2   Geometrical characteristics of the inducers used for validation of the proposed model

	MK1	FAST2	INDUCER A	INDUCER B	INDUCER C	INDUCER D
Number of blades	4	2	3	4	3	3
Tip diameter/mm	168	82.2	127.4	127.4	149.8	174.0
Inlet tip blade angle/deg	82.36	82.62	82.75	82.75	82.5	83.6
Outlet blade angle/deg	73.4 medium	68.76 medium	80.75 tip	80.75 tip	81.0 tip	78.9 tip
Hub/tip at inlet	0.428	0.365	0.300	0.300	0.250	0.287
Hub/tip at outlet	0.69	0.685	0.500	0.500	0.500	0.460
Solidity at tip	2.1	1.59	2.7	3.0	1.91	2.1

grees at the inlet and 20.54 degrees at the outlet, the tip solidity is 1.97 and the design flow coefficient is 0.060.

With reference to the inducer performance evaluation, it is first worth noticing that the numerical solution of the BVP for the discharge velocity profiles and the corresponding closed form approximation lead to essentially equivalent results, as illustrated by the comparison of the noncavitating pumping characteristics shown Fig. 14. Only for significantly low values of the flow coefficient ($\Phi < 0.02$), when the slip velocity becomes comparable to the axial velocity, a small difference between the two curves can be observed.

The model has been validated against the experimental performance of six different tapered-hub inducers, whose main characteristics are summarized in Table 2. Information on inducers A, B, C and D comes from the open Japanese literature. The experimental data concerning inducers A and B have been taken from Hashimoto et. al., 1997[37], and refer to two different LOX pumps. The tests of inducer C are documented in Fujii et. al. , 2002[38]. Finally, inducer D is used in the LE-7A HTP and its experimental performance is reported in Fujii et. al., 2005[39].

Figures 15, 16, 17 and 18 compare the experimental noncavitating characteristics of the MK1, FAST2, A and B inducers with the respective predictions of the simplified closed form solution. The head coefficients based on the static and total pressure, with and without losses, are reported,

together with the "ideal" pumping performance for perfectly guided flow in the absence of pressure losses and deviation effects. For all of these inducers, the static head rise predicted by the model closely agrees with the experimental results.

For better assessment of these results, it is worth noting that the pressure tap used for the measurement of the static head rise developed by the MK1, FAST2, A and B inducers was located more than two diameters downstream of the blade trailing edge. At this location the flow closely approximates the fully-settled axisymmetric conditions necessary for correct comparison of the experimental data with the model predictions. Conversely, Figs. 18 and 19 show that the non-cavitating performance of inducers C and D is evaluated with lower accuracy. Most likely, this situation is related to the different position of the downstream pressure tap, which in this case was located very close to the blade trailing edge. This is clearly inconsistent with the intrinsic nature of the proposed model, whose predictions are specifically derived from consideration of the axisymmetric far-field flow downstream of the inducer. The consequent deviation of the tangential velocity profile from the radial equilibrium introduces a systematic error in the evaluation of the centrifugal effects and, therefore, of the static pressure downstream of the inducer. This is confirmed by the almost linear nature of the measured pumping characteristics of inducers C and D, which is consistent with the expected behavior for nearly uniform distribution of the axial flow velocity at the inducer
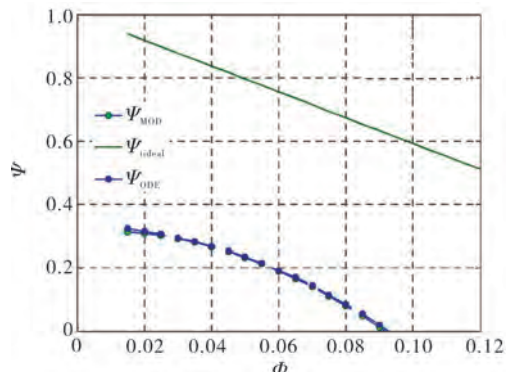

Fig.14   Comparison between the numerical solution (ODE) and the corresponding closed form approximation (MOD) for the noncavitating performance prediction of tapered inducers
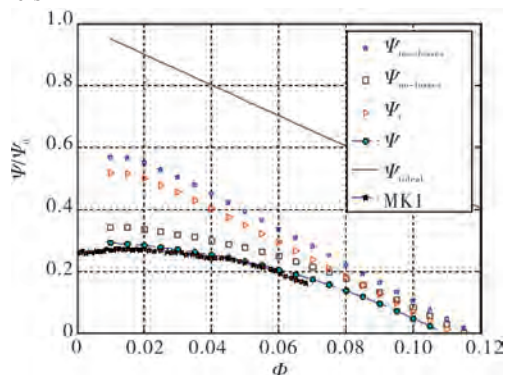

Fig.15   Comparison between the experimental non-cavitating performance of the MK1 inducer (dark stars) and the predictions of the analytical model
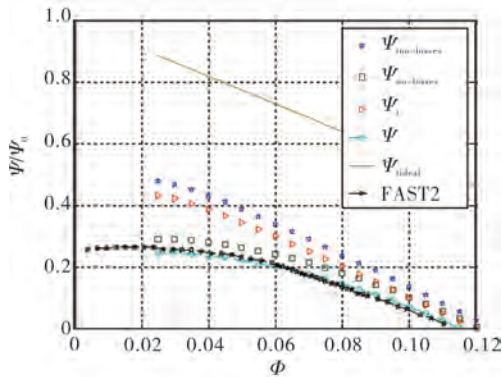
Fig.16　Comparison between the experimental noncavitating performance of the FAST2 inducer (white stars) and the prediction of the analytical model
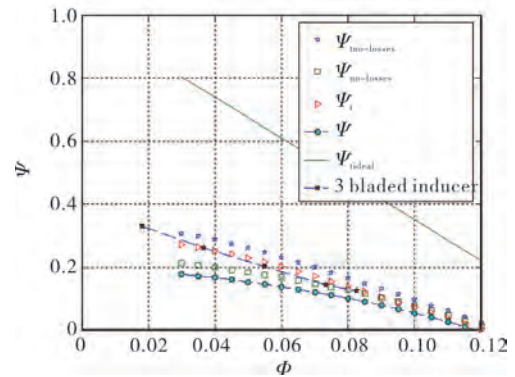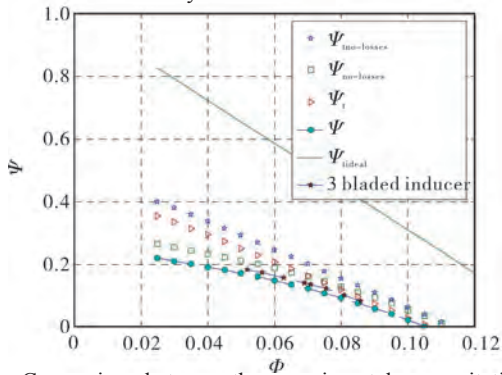

Fig.17　Comparison between the experimental noncavitating performance of the inducer A (dark stars) and the predictions of the analytical model
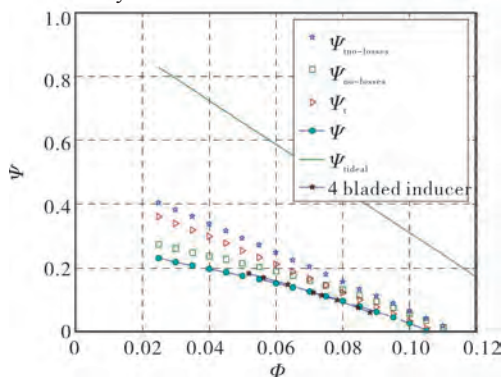

Fig.18　Comparison between the experimental noncavitating performance of the inducer B (dark stars) and the predictions of the analytical model

Fig.19　Comparison between the experimental noncavitating performance of the inducer C (dark stars) and the predictions of the analytical model
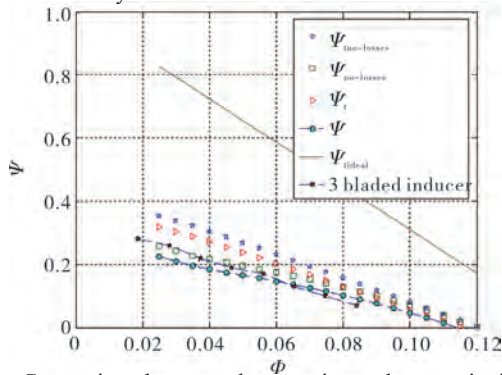

Fig.20　Comparison between the experimental noncavitating performance of the inducer D (dark stars) and the predictions of the analytical model

trailing edge before the establishment of radial equilibrium conditions.

The proposed model can also be applied for predicting the performance of helical inducers of more general hub and blade shapes. However, it is obviously expected to deliver best results when used for geometries more closely consistent with the assumptions used for its derivation, as confirmed by the results for the MK1 and FAST2 inducers.

5　Conclusions

Based on the available evidence, the present theoretical model proved to represent a useful tool for preliminary design and performance analyses of turbopump inducers. More specifically, the model is able to provide accurate quantitative indications for geometry definition, 3D flow field description, characterization and control of the blade loading, and prediction of the noncavitating pumping characteristics of helical inducers with tapered hub and variable blade pitch angle.

In this context, the model can be effectively used in two ways:

·for the preliminary definition of the geometry of tapered inducers, with particular reference to the hub and blade shape in order to minimize secondary flow losses and attain adequate cavitation performance;

·for the preliminary evaluation of the noncavitating performance of an inducer of given shape, or for defining the main geometric characteristics of an inducer, starting from the desired noncavitating pumping characteristic.

More generally, the model provides inducer designers with a comprehensive interpretative framework where the main- often conflicting- aspects of inducer design and their mutual implications can be assessed, quantified and balanced in view of the attainment of the desired requirements and performance.

The tests on the DAPAMITO3 inducer at different tip clearances and water temperatures indicate that the resulting variation of the inducer performance is generated by the modulation of the tip leakage flow and its response to the variations of the liquid viscosity. They also suggested a semi-empirical scaling correction of the inducer head to account

for these effects, and confirmed its validity. This correction has been successfully integrated in the model for more accurate prediction of the non- cavitating performance of high-head axial inducers.

The limitations of the model are mostly related to the simplifying assumptions and approximations introduced in order to attain a practical solution. In particular, improvements in the description of the flow, control of the blade load, and accuracy of the inducer performance prediction are expected to be gained by a more refined treatment of viscous effects, capable to account for the axisymmetric nature of the blade boundary layers and the radial changes of their thickness across the inducer annulus.

ACKNOWLEDGEMENTS

References

[1] Jakobsen J. K., 1971, "Liquid Rocket Engine Turbopump Inducers", NASA SP-8052, Space Vehicle Design Criteria Manuals.

[2] Ashihara K, Goto A.,Kamijo K.,Yamada H.,Uchiumi M.,2002,Improvements of Inducer Inlet Backflow Characteristics Using 3-D Inverse Design Method,Proc.of 38th AIAA/ASME/SAE/ASEE Joint Propulsion Conference, Indianapolis, USA.

[3] Kang D., Cervone A., Yonezawa K., Horiguchi H., Kawata Y., Tsujimoto Y., 2007, "Effect of Blade Geometry on Tip Leakage Vortex of Inducer", Proc. of the 9th Asian International Conference on Fluid Machinery, Jeju, South Korea.

[4] Brennen C. E., 1994, "Hydrodynamics of Pumps", Concepts ETI Inc., Norwich, USA and Oxford University Press, Oxford, GB.

[5] Brennen C. E., 1995, "Cavitation and Bubble Dynamics", Oxford University Press, Oxford, UK.

[6] Lakshminarayana B., 1982, "Fluid Dynamics of Inducers - A Review", ASME J. of Fluids Engineering, 104, pp. 411-427.

[7] Stripling, L.B. and Acosta, A.J., 1962, "Cavitation in Turbopumps-Part 1", ASME J. Basic Eng., Vol. 84, pp. 326-338.

[8] Cooper P., 1967, "Analysis of Single- and Two-Phase Flows in Turbopump Inducers", ASME J. of Engineering for Power, pp. 577-588.

[9] Brennen, C.E., Acosta, A.J., 1973, "Theoretical, Quasi-Static Analysis of Cavitation Compliance in Turbopumps", J. of Spacecraft, Vol. 10, No. 3, pp. 175-179.

[10] Brennen, C.E., 1978, "Bubbly Flow Model for the Dynamic Characteristics of Cavitating Pumps", J. of Fluid Mechanics, Vol. 89, part 2, pp. 223-240.

[11] Tsujimoto, Y., Kamijo, K., Yoshida, Y., 1993, "A Theoretical Analysis of Rotating Cavitation in Inducers", ASME J. of Fluids Engineering, Vol. 115, pages 135-141.

[12] Tsujimoto, Y., Watanabe, S., Horiguchi, H., 1998, "Linear Analyses of Cavitation Instabilities of Hydrofoils and Cascades", Proceedings of US-Japan Seminar: Abnormal Flow Phenomena in Turbomachinery, Osaka, Japan.

[13] Watanabe, S., Yokota, K., Tsujimoto, Y., Kamijo, K., 1999, "Three-Dimensional Linear Analysis of Rotating Cavitation in Inducers Using an Annular Cascade Model", ASME J. of Fluids Engineering, Vol. 121, pp. 866-871.

[14] Semenov, Y. A., Fujii, A., Tsujimoto, Y., 2004, "Rotating Choke in Cavitating Turbopump Inducer", ASME J. of Fluids Engineering, Vol. 126, pp. 87-93.

[15] Pasini A., Torre L., Cervone A., d'Agostino L., 2011, "Continuous Spectrum of the Rotordynamic Forces on a Four Bladed Inducer", ASME J. Fluids Eng. Vol. 133, Iss. 12, December, 2011.

[16] Bramanti C., Cervone A., d'Agostino L., 2007, "A Simplified Analytical Model for Evaluating the Noncavitating Performance of Axial Inducers", Proc. of the 43rd AIAA/ASME/SAE/ASEE Joint Propulsion Conference, Cincinnati, USA.

[17] d'Agostino L., Torre L., Pasini A. and Cervone A., 2008a, "A Reduced Order Model for Preliminary Design and Performance Prediction of Tapered Inducers", 12th Int. Symp. on Transport Phenomena and Dynamics of Rotating Machinery (ISROMAC-12), Honolulu, HI, USA, February 17-22.

[18] d'Agostino L., Torre L., Pasini A., Cervone A., 2008b, "On the Preliminary Design and Noncavitating Performance of Tapered Axial Inducers", ASME J. of Fluids Engineering, Vol. 130, Is. 11.

[19] d'Agostino L., Torre L., Pasini A., Baccarella D., Cervone A., Milani A., 2008c, "A Reduced Order Model for Preliminary Design and Performance Prediction of Tapered Inducers: Comparison with Numerical Simulations", 44th AIAA/ASME/SAE/ASEE Joint Propulsion Conference, Hartford, USA.

[20] Torre L. Pasini A., Cervone A., d'Agostino L., 2009. "Experimental Performance of a Tapered Axial Inducer: Comparison with Analytical Predictions", AIAA Paper 2009-4955, 45th AIAA/ASME/SAE/ASEE Joint Propulsion Conf. & Exhibit, Denver, Colorado, USA, Aug. 2 - 5, ISSN: 0146-3705.

[21] Cervone A., Pace G., Torre L., Pasini A., , S., Agnesi L., d'Agostino L. 2012, "Effects of the Leading Edge Shape on the Performance of an Axial Three Bladed Inducer", 14th Int. Symp. on Transport Phenomena and Dynamics of Rotating Machinery, ISROMAC-14, February 27th-March 2, 2012, Honolulu, HI, USA

[22] d'Agostino L., Pasini A., Valentini D., Pace G., Torre L., Cervone A., 2012, "A Reduced Order Model for Optimal Centrifugal Pump Design", 14th Int. Symp. on Transport Phenomena and Dynamics of Rotating Machinery, ISROMAC-14, February 27th-March 2, 2012, Honolulu, HI, USA.

[23] d'Agostino L., Valentini D., Pasini A., Torre L., Pace G., and Cervone A., 2017a, "On the Preliminary Design and Performance Prediction of Centrifugal Turbopumps-Part 1", in "Cavitation Instabilities and Rotordynamic Effects in Turbopumps and Hydroturbines-Turbopump and Inducer Cavitation, Experiments and Design", d'Agostino L. and Salvetti M.V. (eds.), CISM International Centre for Mechanical Sciences, Courses and Lectures. Vol. 575 No. 1408, Springer, Vien and New York, pp. 136-156,

[24] d'Agostino L., Valentini D., Pasini A., Torre L., Pace G., and Cervone A., 2017b, "On the Preliminary Design and Performance Prediction of Centrifugal Turbopumps-Part 2", in "Cavitation Instabilities and Rotordynamic Effects in Turbopumps and Hydroturbines-Turbopump and Inducer Cavitation, Experiments and Design", d'Agostino L. and Salvetti M.V. (eds.), CISM International Centre for Mechanical Sciences, Courses and Lectures, Vol. 575 No. 1408, Springer, Vien and New York, pp. 157-178.

[25] Cervone A., Testa R., Bramanti C., Rapposelli E., d'Agostino L., 2005, "Thermal Effects on Cavitation Instabilities in Helical Inducers", AIAA J. of Propulsion and Power, Vol. 21, No. 5, pp. 893-899.

[26] Cervone A., Torre L., Bramanti C.,Rapposelli E., d'Agostino L., 2006, "Experimental Characterization of Cavitation Instabilities in a Two-Bladed Axial Inducer", AIAA J. of Propulsion and Power, Vol. 22, No. 6, pp. 1389-1395.

[27] Cervone A., Bramanti C., Torre L., Fotino D., d'Agostino L., 2007, "Setup of a High-Speed Optical System for the Characterization of Flow Instabilities Generated by Cavitation", ASME J. of Fluids Engineering, Vol. 129, Is. 7, pp. 877-885.

[28] Hildebrand F. B., 1976, "Advanced Calculus for Applications", 2nd edition, Prentice Hall, Saddle River, USA.

[29] Lieblein S., Schwenk F. C., Broderick R. L., 1953, "Diffusion Factor for Estimating Losses and Limiting Blade Loadings in Axial Flow Compressor Blade Elements", NACA RM E53D01.

[30] Lieblein S., 1965, "Experimental flow in Two-Dimensional Cascades", in Aerodynamic Design of Axial Flow Compressors, NASA SP-36, pp. 101-149.

[31] Prandtl L., Tietjens O.G., 1934, Applied Hydro- and Aeromechanics, McGraw-Hill Book Co. Inc., New York, USA.

[32] White F.E., 1974, "Viscous Fluid Flow", McGraw Hill.

[33] Rapposelli E., Cervone A. & d'Agostino L., 2002a, "A New Cavitating Pump Rotordynamic Test Facility", 38th AIAA/ASME/SAE/ASEE Joint Propulsion Conf., Indianapolis, IN, USA, July 8-11.

[34] Rapposelli E., Cervone A., Bramanti C. and d'Agostino L., 2002b, "A New Cavitation Test Facility at Centrospazio", 4th Int. Conf. on Launcher Technology "Space Launcher Liquid Propulsion", Liège, Belgium, Dec. 3-6, 2002.

[35] Pace G., Pasini A., Torre L., Valentini D., d'Agostino L., 2012, "The Cavitating Pump Rotordynamic Test Facility at ALTA S.p.A.: Upgraded Capabilities of a Unique Test Rig", 2012 Space Propulsion Conference, May 7-10, 2012, Bordeaux, France.

[36] Yoshida, Y., Kikuta, K., Hasegawa, S., Shimagaki, M., Nakamura, N and Tokumasu, T., 2005, "Thermodynamic Effect on a Cavitating Inducer in Liquid Nitrogen", FEDSM2005-77430, June 19-23, 2005, Houston, TX, USA.

[37] Hashimoto T., Yamada H., Funatsu S., Ishimoto J., Kamijo K., Tsujimoto Y., 1997, "Rotating Cavitation in Three and Four-Bladed Inducers", Proc. of the 33rd AIAA/ASME/SAE/ASEE Joint Propulsion Conference, Seattle, USA.

[38] Fujii A., Azuma S., Yoshida Y., Tsujimoto Y., Horiguchi H., Watanabe S., 2002, "Higher Order rotating Cavitation in a Inducer", Proc. of the 9th Int. Symposium on Transport Phenomena and Dynamics of Rotating Machinery (ISROMAC-9), Honolulu, USA.

[39] Fujii A., Mizuno S., Horiguchi H., Tsujimoto Y., 2005, "Suppression of Cavitation Instabilities by Jet Injection at Inducer Inlet", Proc. of ASME Fluid Engineering Division Summer Meeting and Exhibition (FEDSM2005), Houston, USA.

全文中文摘要

混流空间诱导轮的性能快速交互设计 / Luca d'Agostino

摘要:本文介绍了一种空间推进用混流锥形轮毂诱导轮初步设计和空化性能预测降阶模型的开发与实验验证。该模型通过将二维轴向涡度修正施加到充分导向轴对称流(其轴向速度沿径向均匀分布)上,来描述叶片流道中的三维不可压缩、无粘性、无旋流动。在不忽略径向流动的情况下适当地再定义了叶片的扩压系数,可以控制叶片的负载,并在设计流量系数下预估边界层阻塞和叶片粘性损失,为匹配轮毂型线与叶距角的轴向变化提供一个简单的判据。采用卡特法则计算诱导轮尾缘处的流量偏差。利用质量守恒定律、角动量守恒定律和欧拉方程,推导出了一个简化的二阶边值问题,其数值解定义了诱导轮出口的远场轴对称流速。对攻角、机匣和叶顶间隙损失进行适当的半经验修正,进而得到空化性能。该模型已被证实与在空化泵转子动力学试验装置中测试的两个空间诱导轮的几何和空化特性十分接近,与文献中提到的许多锥形轮毂诱导轮也十分相似。

拉筋形状对离心压缩机排气蜗壳的性能影响 / 王金生 张 龙 张鹏刚 韩 亮 谭佳健 李健伟

摘要:为满足部分离心压缩机组的强度要求,需要在扩压器内增加拉筋。拉筋是连接扩压器的端壁并起支撑作用的组件,然而拉筋的存在必然会导致额外的气动损失,降低压缩机机组的整体效率。本文以某离心压缩机机组的末级为研究对象,采用NUMECA FINE/Turbo软件对叶轮、带拉筋的扩压器和排气蜗壳构成的整级模型进行数值计算,分析并对比三种不同截面形状的拉筋对排气蜗壳的性能的影响。计算结果表明,截面为椭圆形的拉筋对排气蜗壳的气动性能影响最小。

前级叶片安装角对对旋轴流风机的性能影响 / 程德磊 窦华书 毛涵韬 周 炯 吕振海

摘要:为研究两级动叶安装角可调的对旋轴流风机的前级叶片安装角与风机整体性能的匹配机制,本文利用CFD软件,对风机模型进行了三维全流场数值模拟与分析。结果表明:在小流量工况下,适当调小风机的前级叶片安装角可以提高风机的效率;风机在运行过程中,根据当前工况选择合适的安装角,可以有效提高对旋轴流风机的整体性能,改善各流动参数在风机中的分布情况,减少流动损失,扩大工作范围,延迟风机失速和喘振的发生。

规整填料表面气速对气液混流的影响研究 / 王 懿 陈永峰 王晟旻 刘秋实

摘要:为研究规整填料式分离器内流动状况,以垂直平板式规整填料为研究对象,采用不可压Navier-Stokes方程和Phase-Field界面追踪方法,构建了气液混合流动模型,利用数值模拟方法,研究了不同气速对液体降膜流动过程以及气体流动状态的影响。结果表明:气速对液体在降膜流动过程中的成膜有显著影响,不同气速下,会出现三种情况:①部分成膜、部分滴状流动;②成膜时间短暂且液膜很薄,成膜后液膜迅速断裂;③可以形成均匀连续液膜;气速对液膜厚度的影响可忽略;而气速对气体流动状态影响则较为明显,随气速增大,气体将由旋涡式和波浪式的流动逐渐转变为类直线型流动。液体成膜流动,以及气体的类直线型流动有利于气体与液体的充分接触传质,有助于分离过程,该结论可为规整填料式分离器产品的设计改进提供理论依据。

天棚型转子动力吸振器的参数优化 / 刘子良 张 钦 太兴宇 许 琦 姚红良 闻邦椿

摘要:一阶共振响应过大是转子系统普遍存在的问题。提出天棚型转子动力吸振器的概念及结构规划,将其应用于转子一阶共振抑制。利用有限元理论对吸振器-转子耦合系统进行数学建模,并求解频响函数。基于频响函数规划参数的优化数学模型,并利用自适应粒子群优化算法求解。最后,分析了抑振性能对各参数的灵敏度。研究结果表明:天棚型转子动力吸振器能有效降低转子一阶共振振幅;其抑振性能比Voigt型吸振器具有更优异的抑振性能;抑振性能对频率比的灵敏度要远大于阻尼比。

基于叶端定时的转子扭转振动监测方法及系统研究 / 翟功涛 王维民 陈子文 邵 星

摘要:随着变频调速技术在压缩机/风机上的应用越来越广泛,由变频器产生的谐波导致的扭转共振问题也越来越突出。本文提出了一种基于叶端定时的转子扭转振动监测方法,设计并开发了集叶片振动及轴系扭转振动于一体的监测系统。本系统利用脉冲时序计数法处理叶片脉冲序列信息,将相邻叶片实际到达时差与理论到达时差的差值同叶尖角速度相乘得到轴系扭振角位移。实验结果表明,本文提出的基于叶端定时的转子扭转振动监测方法及系统具有可靠的精度,可用于实际工程测试,为旋转机械扭振测量提供新途径。